Ventilation performance evaluation of an operating room with temperature-controlled airflow system in contaminant control

A numerical study

Hu, Nan; Lans, Jos; Gram, Annika; Luscuere, Peter; Sadrizadeh, Sasan

DOI
10.1016/j.buildenv.2024.111619

Publication date
2024

Document Version
Final published version

Published in
Building and Environment

Citation (APA)
Hu, N., Lans, J., Gram, A., Luscuere, P., & Sadrizadeh, S. (2024). Ventilation performance evaluation of an operating room with temperature-controlled airflow system in contaminant control: A numerical study. *Building and Environment*, *259*, Article 111619. https://doi.org/10.1016/j.buildenv.2024.111619

Building and Environment 259 (2024) 111619

Contents lists available at ScienceDirect

Building and Environment

journal homepage: www.elsevier.com/locate/buildenv

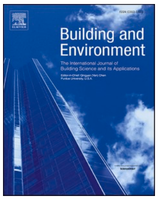

Ventilation performance evaluation of an operating room with temperature-controlled airflow system in contaminant control: A numerical study

Nan Hu[a,*], Jos Lans[b,c], Annika Gram[a], Peter Luscuere[b], Sasan Sadrizadeh[a,d]

[a] *Department of Civil and Architectural Engineering, KTH Royal Institute of Technology, Sweden*
[b] *Faculty of Architecture and the Built Environment, Delft University of Technology, the Netherlands*
[c] *Reinier de Graaf Hospital, Delft, the Netherlands*
[d] *School of Business, Society and Engineering, Mälardalen University, Sweden*

ARTICLE INFO

Keywords:
Operating room
Temperature-controlled ventilation
Contaminant dispersion
Numerical simulation

ABSTRACT

This article investigates the efficacy of temperature-controlled airflow systems in modern operating rooms for contaminant control, a critical factor in preventing surgical site infections. We have conducted experimental measurements in an operating room equipped with temperature-controlled ventilation to map the airflow field and contaminant dispersion (airborne particles with diameters ranging from 0.5 to 1 μm). The results were used to validate the computational fluid dynamics code, which was then employed to simulate and examine different conditions, including contaminant release locations and air supply rates. Realizable k-epsilon and passive scalar models were utilized to simulate airflow and airborne particle phases. We assessed the airflow distribution and contaminant dispersion, utilizing indices such as ventilation and air change efficiency scales. The analysis provided quantitative insights into the distribution and removal of contaminants, as well as the speed at which the room air was replaced. Contamination was found to be effectively reduced when contaminants were released near exhaust outlets or under central unidirectional inlets. The presence of the operating table caused a big distortion of the central downward airflow, forming a horizontal air barrier at the periphery. Under this unique interior configuration, an appropriate air supply ratio between central and periphery zones was required to achieve optimal overall ventilation performance.

Nomenclature

C_0	Volume integral of the contaminant concentration throughout the room (kg)
C_1, C_2, $C_{1\varepsilon}$, $C_{3\varepsilon}$	Model coefficients (–)
C_p	Contaminant concentration at cell p (kg/m^3)
C_s	Representative concentration (kg/m^3)
d_c	Characteristics dimension of the obstacles (m)
D_m	Mass diffusivity (m^2/s)
d_p	Particle diameter (m)
D_T	Thermal diffusivity (m^2/s)
F	Body force per unit mass (m/s^2)
G_i	Gravity center coordinate (m)
G_k, G_b	Turbulent kinematic energy production terms (J/m^3/s)
k	Turbulent kinematic energy (J/kg)
P	Static pressure (Pa)

(*continued on next column*)

(*continued*)

q	Contaminant generation rate (kg/s)
Q	Volumetric supply flow rate (m^3/s)
Sct	Turbulent Schmidt number (m^2/s)
S_k, S_ε, S_Y	Source term (kg/m/s^3, kg/m/s^4, kg/m^3/s)
t	Time (s)
T	Temperature (K)
U_i	Mean velocity (m/s)
U_∞	Free-stream fluid velocity (m/s)
V	Room volume (m^3)
V_p	Volume of cell p (m^3)
x_i	Spatial coordinate (m)
X_i	Center coordinate of cell p (m)
Y	Contaminant mass fraction (–)
Y_p	Contaminant mass fraction at cell p (–)
$Y_p(0)$	Initial contaminant mass fraction in cell p (–)
$Y_p(t)$	Contaminant mass fraction at time t in cell p (–)

(*continued on next page*)

---

[*] Corresponding author.
E-mail address: nanhu@kth.se (N. Hu).

https://doi.org/10.1016/j.buildenv.2024.111619
Received 20 February 2024; Received in revised form 29 April 2024; Accepted 5 May 2024

(*continued*)

Greek letters	
δ_{ij}	Kronecker delta
ε	Dissipation rate (m^2/s^3)
ε_a	Contaminant removal efficiency (–)
μ	Dynamic viscosity (kg/m/s)
μ_t	Turbulent viscosity (kg/m/s)
ν	Kinematic viscosity (m^2/s)
ρ	Fluid density (kg/m^3)
ρ_d	Particle density (kg/m^3)
$\rho_{mixture}$	Density of air-contaminant mixture (kg/m^3)
σ_ε, σ_k	Model coefficients (–)
τ_n	Nominal time constant (s)
τ_p	Local age of the air (s)
Subscripts and Abbreviations	
ACE	Air Change Efficiency
BC(s)	Boundary Condition(s)
BCPs	Bacterial-Carrying-Particles
CAD	Computer-Aided Design
CDC	Centers for Disease Control
CFD	Computational Fluid Dynamics
CRE	Contaminant removal effectiveness
CRW	Continuous Random Walk
DNS	Direct Numerical Simulation
DRW	Discrete Random Walk
G	Gravity Center
H	Height
HAIs	Hospital-Acquired Infections
L	Length
LAF	Laminar Airflow
LED	Light-Emitting Diode
LES	Large Eddy Simulation
OR(s)	Operating Room(s)
RANS	Reynolds-Averaged Naiver-Stokes
RMSE	Root Mean Square Error
SSIs	Surgical Site Infections
Stk	Stokes number
SVE1	Scale for Ventilation Efficiency 1
SVE2	Scale for Ventilation Efficiency 2
TcAF	Temperature-controlled Airflow
TMA	Turbulent Mixing Airflow
UDAF	Unidirectional Airflow
UDF	User-Defined Function
UDM	User-Defined Memory
W	Width

1. Introduction

According to previous prevalence surveys and progress reports on hospital-acquired infections (HAIs) published by Centers for Disease Control (CDC), surgical site infections (SSIs) have been the most common and costly HAI type, posing a substantial burden on public health [1–3]. To mitigate this healthcare challenge, infection control in ORs where surgical wounds are created plays a critical role. Early in the 1980s, abundant statistical research demonstrated the crucial link between a clean OR environment and the prevention of SSIs and revealed the effectiveness of ventilation technology in infection control for ORs [4,5]. Through clean and well-organized airflow streams, OR ventilation systems supply direct and continuous control of airborne pathogens, reducing the concentration level of air contamination and minimizing the incidence of infection.

Two types of conventional ventilation systems in ORs are turbulent mixing airflow (TMA) and laminar airflow (LAF) [6–8]. TMA primarily utilizes the ceiling-level air supply and floor-level air extract on side walls. A Large volume of clean air with high momentum is introduced with the aim of fully mixing with indoor air and diluting the contaminants in OR environments. LAF features a large air supply section throughout the whole ceiling area and flushes the contaminated indoor air away from the surgical zone to the floor-level exhaust grills. On the basis of these traditional ventilation systems, a hybrid ventilation system called temperature-controlled airflow (TcAF) has been recently developed and installed in several modern ORs [8]. It incorporates decentralized mixing air supply in the periphery zone and concentrated unidirectional airflow in the central zone. In addition, the central air supply is kept 1–3° cooler than the desired room temperature, and the warmer periphery air regulates the OR temperature. The temperature gradient between two air supply sections enhances both the central downward airflow and the surrounding air mixing. In TcAF, the combination of TMA and LAF, as well as the utilization of buoyancy effect, aim to maximize performance and reduce operation costs. The novel ventilation strategy enhances infection control and aligns with global efforts to reduce energy consumption and carbon emissions in healthcare settings. As illuminated by Brenda et al. [9], the quest for infection control within ORs unites with the broader imperative for energy-efficient healthcare buildings. Advanced ventilation technologies like TcAF play an important role in achieving sustainable, green healthcare infrastructures without compromising hygiene standards or user comfort.

Several studies compared TcAF with conventional ventilation principles in OR environments. Alsved et al. measured viable airborne bacterial loads in three ORs equipped with TMA, LAF and TcAF and summarized that TcAF maintains very low levels of microbiological organisms in air with moderate air delivery [10]. Subsequent numerical studies confirmed the superiority of TcAF through the analysis of the spatial bacterial-carrying-particles (BCPs) concentration [11,12]. The existing literature suggests that TcAF can serve as an alternative to traditional ventilation principles. Meanwhile, they highlighted the significant role of airflow patterns in contaminant control performance and revealed the potential factors such as room layout and ventilation rate, etc.

In addition to critical physical properties, ventilation performance metrics are of great interest. It enables a straightforward understanding of the effectiveness of ventilation systems and easy benchmarking and comparison for system design and optimization. Cao et al. [13] summarized different assessment indices in terms of air exchange, pollutant removal, heat removal, exposure to contaminants, and airflow distribution. Considering the protective purpose of ventilation in OR, metrics describing local air quality or contamination level are commonly used. It includes air change efficiency (ACE), mean age of air, contaminant removal effectiveness (CRE), net escape velocity, purging flow rate, purge time, scales for ventilation efficiency, spread index, and visitation frequency [14–23]. These metrics serve to evaluate two main aspects of ventilation: air replacement and contaminant removal. The first two indicators, ACE and mean age of air, pertain to air replacement, measuring the system's capability to introduce fresh air and expel stale air. On the other hand, the remaining metrics focus on contaminant removal effectiveness, accounting for the characteristics of contaminant sources to assess ventilation performance in removing pollutants from the indoor environment. TcAF, as a novel ventilation technology, lacks comprehensive and in-depth quantitative analysis, particularly in terms of its non-uniform airflow pattern and contaminant distribution. Two scales of ventilation efficiency, namely SVE1 and SVE2, are selected to investigate the mechanisms by which TcAF eliminates contaminants released from various locations. Compared to other contaminant removal indicators, SVE1 and SVE2 offer a more detailed quantitative depiction of both contamination level and spatial dispersion range. In terms of TcAF's response to inadequate or imbalanced air delivery, the authors opt for customary measures, ACE and mean age of air, due to their broad applicability.

It is also worth noting that OR geometries and configurations in previous studies were often idealized and outdated. However, contemporary ORs significantly differ from their older counterparts. For instance, an image-guided system now commonly installed at the floor or ceiling compromises the flexibility of arranging air showers and obstructs the introduced airflow. The critical role of room layout on ventilation performance is acknowledged, yet TcAF's ventilation performance in modern ORs with realistic configurations remains unclear.

This study aims to enhance comprehension regarding the spatial variability of contaminant control capacity within modern ORs utilizing the TcAF system and advances the knowledge related to the design of TcAF's air supply strategy. This paper offers a comprehensive numerical and experimental investigation analyzing the airflow distribution and contaminant dispersion in a recently built OR equipped with a TcAF system. Experimental measurements have been conducted on the air velocity, temperature, and aerosol particle diffusion throughout the OR under the standard TcAF operation, while computational fluid dynamics (CFD) simulations investigated various contaminant release positions and ventilation rates. Moreover, the contaminant control performance of TcAF under diverse working conditions was quantitatively assessed using specific ventilation effectiveness indices.

2. Method

2.1. OR layout descriptions

OR at Rijnstate Hospital in the Netherlands (see Fig. 1a) was selected for full-scale numerical and experimental investigations to evaluate its actual performance. The OR measures 11.6 m in length (L), 6.4 m in width (W), and 3.0 m in height (H). In the OR's center, air flows downward from three unidirectional airflow (UDAF) plenums comprising seven half-spherical air diffusers. Along the periphery, 18 diffusers, arranged in parallel, distribute filtered air across the remaining space. This configuration creates two zones (central and periphery), each with an equal air supply of 6300 m^3/h. Consequently, with a uniform surface size of 0.18 m^2, internal air showers receive 300 m^3/h, whereas external air showers are supplied 350 m^3/h. Four exhaust grills, measuring 0.95 m in width (W) by 0.5 m in height (H), are located on the side walls at floor level. The air introduced above the operating table is colder by 1 K than the OR's ambient temperature. This temperature difference is achieved by regulating the supply temperature from 18 diffusers in the periphery zone. Illumination in the OR is provided by 17 ceiling-mounted square LED panels (0.6 m × 0.6 m) scattered around the periphery zone and six additional rectangular LED panels (1.2 m × 0.2 m) placed between three UDAF plenums. Furthermore, two surgical lamps, each with a radius of 0.3 m, are suspended symmetrically 2.2 m above the floor, with a 0.6 m offset from the operating table's centerline. The OR includes medical equipment such as an anesthesia machine, an endoscopy tower, and an image-guided therapy system (C-arm). The imaging system, integrated with a carrier, is ceiling-mounted via a rail system, and positioned in its parking configuration. A CAD model replicates the examined OR's interior layout, incorporating appropriate geometric simplifications illustrated in Fig. 1 b.

2.2. Numerical model

This study investigates the airflow movement and airborne particle distribution within the OR environment using ANSYS Fluent 2021, a commercially available CFD software. A reference simulation case has been established for verification and validation purposes, replicating the experimental setup in the Rijnstate Hospital OR, Netherlands. Additionally, a series of simulations were conducted to assess the contaminant control performance of TcAF under various system configurations.

2.2.1. Airflow model

Simulating indoor airflow accurately and reliably has long been a challenging endeavor due to its turbulent nature characterized by chaotic and disordered fluid motion. Direct Numerical Simulation (DNS) and Large Eddy Simulation (LES) could capture the transient flow features but require intensive computational resources. In contrast, the Reynolds-Averaged Navier-Stokes (RANS) method is a more practical scheme, offering a well-balanced combination of robustness, computational efficiency, and accuracy [24]. This method decomposes flow variables into time-averaged and fluctuating components. The flux due to turbulent fluctuations, known as the Reynolds stress term, requires additional modeling to achieve closure in the equation system. One commonly used approach for modeling turbulent stress is the eddy-viscosity hypothesis. Among the various eddy-viscosity turbulence models, the Realizable k-ε model has been widely applied for airflow simulation in ventilated rooms and has shown good performance in predicting particle flow [25,26]. Consequently, the Realizable k-ε model has been employed, and the reliability of the predicted results has been carefully validated through comparison with experimental data. Assuming a Newtonian, incompressible flow, the time-averaged transport equations for mass, momentum, turbulent kinetic energy, and turbulent dissipation rate are expressed in Eqs. (1)–(4)

$$\frac{\partial(\rho u_i)}{\partial x_i}=0 \tag{1}$$

$$\frac{\partial(\rho u_i)}{\partial t}+\frac{\partial(\rho u_i u_j)}{\partial x_j}=-\frac{\partial P}{\partial x_i}+\frac{\partial}{\partial x_j}\left[(\mu+\mu_t)\left(\frac{\partial u_i}{\partial x_j}+\frac{\partial u_j}{\partial x_i}\right)-\frac{2}{3}k\rho\delta_{ij}\right]+\rho F_i \tag{2}$$

$$\frac{\partial(\rho k)}{\partial t}+\frac{\partial(\rho k u_j)}{\partial x_j}=\frac{\partial}{\partial x_j}\left[\left(\mu+\frac{\mu_t}{\sigma_k}\right)\frac{\partial k}{\partial x_j}\right]+G_k+G_b-\rho\varepsilon+S_k \tag{3}$$

$$\frac{\partial(\rho\varepsilon)}{\partial t}+\frac{\partial(\rho\varepsilon u_j)}{\partial x_j}=\frac{\partial}{\partial x_j}\left[\left(\mu+\frac{\mu_t}{\sigma_\varepsilon}\right)\frac{\partial\varepsilon}{\partial x_j}\right]+\rho C_1 S\varepsilon-\rho C_2\frac{\varepsilon^2}{k+\sqrt{\nu\varepsilon}}+C_{1\varepsilon}\frac{\varepsilon}{k}C_{3\varepsilon}G_b+S_\varepsilon \tag{4}$$

Here, ρ represents the fluid density, t is time, u_i and x_i are mean velocity,

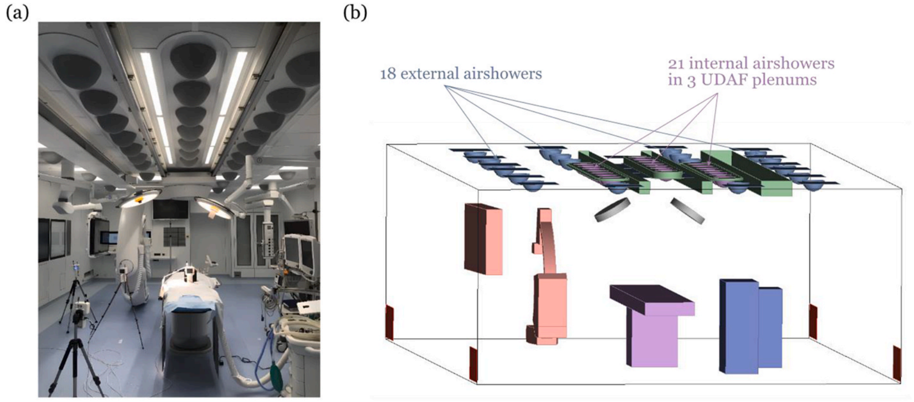

Fig. 1. a) Interior view of the state-of-the-art OR at Rijnstate Hospital, Netherlands; b) the replica CAD model.

and the spatial coordinate in the ith direction. The terms P, μ, and μ_t denote mean static pressure, dynamic viscosity, and turbulent viscosity, respectively. k represents turbulent kinematic energy, δ_{ij} is the Kronecker delta, and F is the body force per unit mass. G_k and G_b are the turbulent kinematic energy production terms due to mean velocity gradients and buoyancy, respectively. ε is the dissipation rate, S_k and S_ε are source terms, and ν is the kinematic viscosity. The parameters σ_ε, σ_k, C_1, S, C_2, $C_{1\varepsilon}$, $C_{3\varepsilon}$ are model coefficients, with their specific values or expressions detailed in the ANSYS Fluent Theory Guide [27].

This study models a steady airflow field, neglecting the time derivative term in the equations. The Convective term is discretized using a second-order upwind scheme. To handle the staggered pressure and velocity grids, the PRESTO! pressure interpolation scheme is employed. In the iterative process, momentum and pressure-based continuity equations are simultaneously solved using the Coupled algorithm. Three convergences criteria are established: achievement of mass and energy balance, attainment of stable temperature solutions at monitor planes/points, and residuals below 10^{-3} (for energy, the convergence criteria are 10^{-6}). These criteria ensure the accuracy and stability of the simulation results.

2.2.2. *Contaminant dispersion model*

Two prominent numerical methods, Eulerian and Lagrangian models, are commonly employed for simulating contaminant dispersion in indoor environments. In the Eulerian approach, the focus is on the concentration of particles, calculating the overall diffusion and convection of a number of particles, which is particularly effective for simulating the fine particle dispersion in environments with high air exchange rates as observed in the OR. In contrast, the Lagrangian approach, which deals with individual particles and calculates the trajectory of each particle separately, is often preferred in usual enclosed environments with larger particles and lower airflow rates.

In our experiment, the measured particles have a density of 900 kg/m^3 and a diameter of 0.5 μm. The Stokes number (Stk) is calculated to be 1.7e-7 based on Eq. (5).

$$Stk = \frac{\rho_p {d_p}^2 U_\infty}{18 \mu d_c} \tag{5}$$

Where ρ_p and d_p are the density and diameter of the particle, U_∞ is the free-stream fluid velocity, μ_g represents the dynamic viscosity of the fluid phase and d_c is the characteristic dimension of the obstacles.

A Stokes number significantly below 0.1 indicates that particles closely follow fluid streamlines [17]. Under these conditions, airflow is the primary driving force, with minimal influence from gravity and inertia [18,19]. Furthermore, given the high air exchange rate in the OR, deposition loss of fine particles on solid surfaces is negligible [19,20]. Given such conditions, tracer particles exhibit dynamic characteristics akin to gaseous species.

While the Lagrangian model offers detailed insights into particle dynamics [28], it is less suited to the conditions of our experiment where fine particles closely follow fluid streamlines. Therefore, this paper employs a Eulerian model, specifically a species transport model, to determine the contaminant distribution. The governing equation for the tracer species is expressed in Eq. (6).

$$\frac{\partial(\rho Y)}{\partial t} + \frac{\partial(\rho Y u_j)}{\partial x_j} = \frac{\partial}{\partial x_j}\left[\left(\rho D_m + \frac{\mu_t}{Sc_t}\right)\frac{\partial Y}{\partial x_j} + \frac{D_T}{T}\frac{\partial T}{\partial x_j}\right] + S_Y \tag{6}$$

In this equation, Y signifies the local mass fraction of the species, ρ is the fluid density, t is time, and T is the temperature. u_j and x_j are the velocity component and the spatial coordinate in the jth direction, respectively. D_m and D_T refer to mass and thermal diffusivity. μ_t is the turbulent viscosity, and Sc_t is the turbulent Schmidt number, which is the ratio of kinematic viscosity and mass diffusivity. S_Y represents the source term.

To validate the model, simulations of steady tracer release and transient tracer decay were conducted. A user-defined function (UDF) was employed to define the release location, and a constant source flux in kg/s was specified. Following computation of a converged steady-state airflow field, the species transport equation was iterated until achieving a stable tracer concentration distribution within the computational domain. This stable concentration distribution served as the initial condition for the subsequent tracer decay simulation. The simulation was then switched to transient mode, deactivating the source term to model tracer decay. A time step size of 1 s was assigned for the transient simulation.

2.2.3. *Mesh and boundary conditions*

To account for the complex geometry of the OR, we have adopted an unstructured space discretization strategy for grid generation. All surfaces are initially covered with a triangle mesh, with individual maximum size settings to ensure accuracy. This surface mesh is then converted into a tetrahedral grid to fill the computational domain. Three prism layers are created to capture the flow physics in the boundary layer better and accurately calculate the particle deposition. As we have used enhanced wall treatment, the thickness of the first layer is controlled to ensure that the y + value is lower than 5. In addition, we have performed grid-independence tests with three different grid resolutions (5.4, 9, and 15 million cells) to ensure that the grid resolution does not influence the simulation outcomes [29,30]. Velocity and temperature profiles along the centerline of the long side of the OR are plotted in Fig. 2, revealing negligible differences between the medium and fine mesh resolutions. As a result, a grid with 9 million cells seems fine enough and thus chosen for our simulations.

A no-slip condition is applied to all solid surfaces in the OR, including walls, ceiling, floor, lamps, and medical devices. Velocity inlets are assigned to both internal and external air showers, while the four exhausts are specified as outflow boundaries. The ceiling lights are subjected to a constant heat flux. The surgical lamps' bottom and top surfaces are set to their respective measured operating temperatures. All remaining solid surfaces are treated as adiabatic, indicating no heat transfer occurs through these surfaces. Details of the boundary conditions for the reference scenario are provided in Table 1.

2.2.4. *Ventilation performance indices and simulation cases*

The primary objective of ventilation in ORs is to ensure a healthy indoor environment for both patients and healthcare providers during surgical procedures, with a particular emphasis on air cleanliness and contaminant control [8]. In order to evaluate the TcAF ventilation performance, we consider different locations and scales of contaminant release and select appropriate assessment indices. First, we designated individual point sources in the OR equipped with the TcAF system under standard air supply conditions. To assess the elimination of passive contaminants released from these fixed points by the TcAF system, the scale for ventilation efficiency 1 (SVE1), center gravity for contaminant distribution (G), and scale for ventilation efficiency 2 (SVE2), indices proposed by Kato and Murakami [17]. The SVE1 index represents the spatial average contaminant concentration, while the G and SVE2 indices specify the concentration centroid and the mean radius of contaminant diffusion. These indices quantify the contaminant removal capacity of the ventilation at different locations and provide a clear and concise description of the spatial distribution. In comparison to conventional measures such as local contaminant removal efficiency (ε_a in Ref. [31]) or complex contaminant contours, these indices provide more informative and quantitative insights.

Secondly, the TcAF system's response to contaminant sources of unknown scales and locations was analyzed by examining the local mean age of air (τ_p) or the local air change efficiency (ACE). The local mean age of air is defined as the average time it takes for a fluid parcel to travel from the inlet to a particular point. For the region with inactive air movement and mixing, its air age tends to be older. Therefore, the concept of air age gives a reflection of the airflow pattern in the

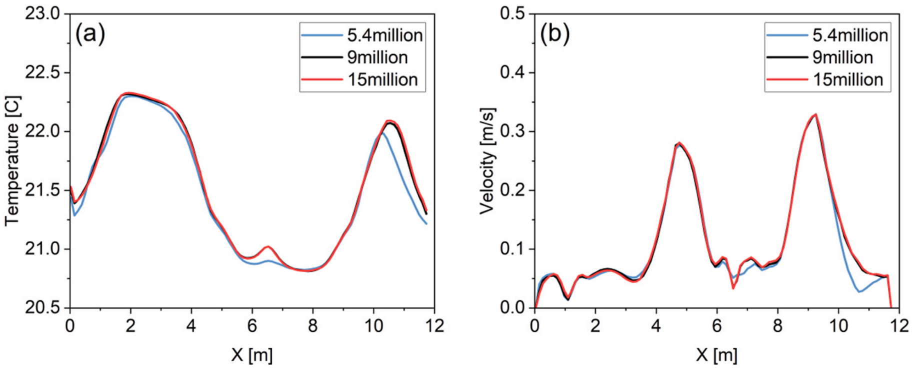

Fig. 2. Comparative analysis of temperature and velocity distributions for three distinct grid resolutions.

Table 1
The simulated parameters defined in the reference case.

Objects	Size [m^2]	BC type	Thermal BC	Momentum BC	Species BC
Internal air showers	0.18 × 21	Velocity-inlet	293.65 K	0.48 m/s	0
External air showers	0.18 × 18		295.15 K	0.55 m/s	0
Outlets	0.48 × 4	Outflow	–	–	–
Anesthesia	4.03	Wall	160 Watt	No-slip	Zero diffusive flux
Endoscopy	3.09		230 Watt		
C-arm	5.75		0 heat flux		
C-arm screen	4.49				
Operating table	10.97				
Room walls	–				
Room ceiling	–				
Ceiling structure	–				
Room floor	–				
Surgical lamp	0.71 × 2		Top surface: 321.15 K, Bottom surface: 297.15 K		
Ceiling square light	0.36 × 17		30 Watt per lighting panel		
Ceiling bar light	0.18 × 6				
Tacer generation	6.94e-7 kg/s tracer flux from a single cell at the specific releasing location.				

ventilated room [32]. It is assumed that the age of air at the inlet equals zero. After the air enters the room, it is a mixture of fresh air and recirculated air. Older air age corresponds to a higher ratio of recirculated air, therefore indicating the freshness of the air and the dilution capacity at a specific point. Kato and Murakami [17] defined a new ventilation performance parameter called scale for ventilation efficiency 3 (SVE3) with the same physical meaning as the local mean age of air. In this context, the fluid parcel is considered as the fresh clean air entering through inlets, and SVE3 corresponds to the mean traveling time required by the fluid parcel to reach the point concerned. The local mean age of air can be obtained by either experimental measurements or simulations. According to Sandberg and Sjoberg [16], its expression varies with different injection procedures. As for SVE3, it is a "virtual concept" based on the simulated results and cannot be directly measured in practice. Under uniform and continuous contaminant generation throughout the room, the supplied air mass is gradually contaminated, and its concentration is proportional to the mean traveling time, i.e., SVE3. Therefore, SVE3 corresponds to an expression of the age-of-air concept under a steady-state uniform injection procedure.

On the basis of the age-of-air concept, the local ACE index was proposed by Etheridge and Sandberg [19], and widely utilized for quantifying the airflow pattern features. It is defined as the ratio between the nominal time constant (τ_n) and the local mean age of air (τ_p). The theoretical concept τ_n represents perfect mixing airflow distribution, corresponding to the shortest possible mean age of air. The local ACE offers direct information on air quality at specific locations, indicating if the air is too old and indirectly reflecting contamination potential. This index, based solely on the airflow pattern, remains independent of the contaminant release state [33]. At the same time, it maintains a straightforward relationship with contaminant control. Regions exhibiting low ACE values indicate inadequate air exchange, posing risks of contaminant accumulation and unsatisfactory contaminant removal performance.

For calculating SVE1 and SVE2, a steady tracer release simulation was conducted, and a UDF compiled to specify the source location and strength. The relevant functions used in the simulation are defined as follows:

$$C_s = \frac{q}{Q} \tag{7}$$

$$SVE1 = \frac{C_0}{C_s V} = \frac{\int_V C_p dV_p}{C_s V} = \frac{\int_V \left(Y_p \rho_{mixture}\right) dV_p}{C_s V} \tag{8}$$

$$G_i = \int_V \frac{X_i C_p}{C_0} dV_p \tag{9}$$

$$SVE2 = \sqrt{\frac{\int_V (X_i - G_i)^2 C_p dV_p}{C_0}} \tag{10}$$

Here, C_s represents the representative concentration, equal to the average concentration at the exhaust, q is the contaminant generation rate, and Q signifies the total volumetric flow rate supplied to the room. C_0 is the volume integral of the contaminant concentration throughout the room. C_p, V_p and Y_p correspond to the contaminant concentration, volume, and contaminant mass fraction of cell p, respectively. V is the room volume, while $\rho_{mixture}$ represents the density of the air-contaminant mixture. G_i indicates the gravity center coordinate for contaminant distribution, and X_i is the center coordinate of cell p (i = 1,2,3). During post-processing, these indices were computed utilizing custom field functions.

Various methods determine the age of air distribution in enclosed rooms, including the step-up injection, step-down, steady-state, and particle-marker methods [14]. In this study, the step-down method, involving a transient tracer decay process, was employed. Using a uniform mass fraction of a tracer contaminant as the initial condition, Eq. (6) was iterated over time without source generation, based on a frozen airflow field. The local age of the air of a single cell can be found from:

$$\tau_p = \int_0^\infty \frac{Y_p(t)}{Y_p(0)} dt \tag{11}$$

Where, τ_p is the local age of the air within a single cell p, $Y_p(t)$ is the mass fraction of a tracer contaminant at time t in the cell p, and $Y_p(0)$ is the initial mass fraction of the tracer in cell p. A time integral for each cell in the fluid zone is calculated using a User-Defined Function (UDF) and stored in User-Defined Memory (UDM). To illustrate the disparity in air exchange ability among the central, periphery, and whole OR, the respective volume-averaged age of the air is also calculated.

This study initially investigated the non-uniform contaminant control capabilities of the TcAF system, equipped with a standard airflow supply. To capture regional variations, twelve contaminant release locations were considered, six in the periphery and six in the central area of the OR. The spatial variability of the TcAF system, in terms of air exchange and cleanliness, was further explored using the air-age distribution theory, without specifying contaminant sources. Additionally, four more ventilation rates were examined to assess the system's performance under inadequate or imbalanced air supply conditions. Overall, 16 simulation scenarios were studied, as outlined in Table 2.

2.3. Experimental setup

Two objective experiments were conducted in the hybrid OR, as described in Section 2.1: a). temperature and velocity measurement; and b). tracer particle decay measurement. An 'at-rest' situation, with equipment installed and operating in a customers manner and no personnel present, is considered in such experiments. Specifically, medical equipment and surgical lights were activated and positioned as per operational standards (DIN 1946-4 [34]) while the C-arm remained in its parking position. Prior to conducting measurements, a technical inspection of the TcAF system ensured its functional integrity. Furthermore, TcAF operational parameters, such as supply air temperature and flow rate, were pre-set to guarantee stable measurement conditions. Given the TcAF system's sensitivity to horizontal variations in temperature and velocity over vertical trends, 48 monitoring points (see Fig. 3) were strategically placed around the OR at a height of 1.20 m above the floor level, in accordance with ISO14644-3 [35]). Measurements were taken using a TSI 966 thermoanemometer articulated probe, with a range of 0–50 m/s and −10 to 60 °C, a resolution of 0.01 m/s and 0.1 °C, and an accuracy of ±0.015 m/s and ±0.3 °C, at each location for 3 min with 15-s intervals. This experimental data later served to validate the airflow field in the results section.

The tracer particle decay experiment, conceived to assess the recovery rate, was conducted in accordance with ISO 14644-3 [35]. Within the OR, a calibrated Topas aerosol generator (model ATM 226) was strategically positioned at a release point 1.8 m above the floor level, as denoted by the star mark in Fig. 3). Particle number concentration, for particles of size greater than 0.5 μm) at six monitoring points situated 1.2 m above the floor level (P1–P6), was quantified using Lighthouse 3016 handheld particle counters, operating at a flow rate of 2.83 l/min. The substance utilized, ATI PAO-4 (chemically identified as 1-Decene, homopolymer, hydrogenated, or 1-Decene, tetramer mixed with 1-decene), was atomized into spherical aerosols ranging in size from 0.5 to 1 μm, and subsequently discharged into the OR to establish a background concentration. The emission was halted once all particle counters (with the exception of P6, positioned under the UDAF) indicated a concentration ≥ 10^7 particles/m^3. A 10-min decay process at the six monitoring points was documented, employing a measuring cycle of 1 min. This manuscript leverages experimental data for the verification of the contaminant dispersion field.

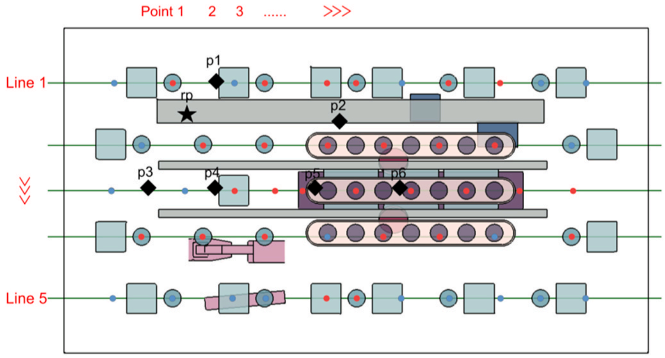

Fig. 3. Measurement setup, illustrating temperature and velocity monitoring points, represented by blue and red points respectively (48 in total). The location for particle release is denoted by a black star, while particle concentration monitoring points (6 in total) are indicated by black diamonds. (For interpretation of the references to colour in this figure legend, the reader is referred to the Web version of this article.)

Table 2
Details of different scenarios.

Parametric study			
Independent variable	Parameter range		Aims and indices
Single-point contaminant source	Case E1–E6	Located in the periphery	Contaminant removal efficiency: SVE1, SVE2
	Case CM, C1–C5	Located in the central zone	
Supply airflow [m^3/h]	Case 1	300/350[a]	Air change efficiency: Mean age of air
	Case 2	225/262.5[a]	
	Case 3	150/175[a]	
	Case 4	300/175[a]	
	Case 5	150/350[a]	

[a] The first value indicates the supply flow rate for internal air showers, whereas the second value refers to the supply flow rate designated for external air showers situated in the periphery area of the OR.

3. Results and discussion

3.1. Numerical model validation

Before conducting parametric studies to evaluate the TcAF system's efficacy, validating the employed numerical models is imperative. To this end, a comparison of representative indoor air and contaminant characteristics was conducted between simulation outcomes and experimental data.

Given the turbulent nature of the OR's airflow field, air velocity measurements exhibited fluctuations during the 3-min measurement period, whereas temperature variations were comparatively minor. A preliminary analysis of the velocity measurement data facilitated the identification of 28 out of 48 points (indicated by red points in Fig. 3) that satisfied the criteria for steady-state measurements, rendering them suitable for validation purposes.

Fig. 4 compares the simulated temperature and air velocity at a floor level of 1.2 m against the corresponding experimental data. The comparison reveals a commendable concordance between the simulation and experimental findings. Nevertheless, minor variances were noted at line 2, point 5 (adjacent to the Anesthesia and Endoscopy devices), line 3, points 3 and 4, along with line 4, points 4 and 5 (in proximity to the two surgical lamps). These variances are likely attributable to minor geometrical divergences between the replica CAD model and the actual physical setup.

Simulations of tracer particle release and decay were conducted to validate the contaminant dispersion field, adhering to the setup depicted in Fig. 3. To facilitate a more accurate comparison between experimental data and simulation outcomes, concentration values were normalized against the average concentration observed at all six monitoring points.

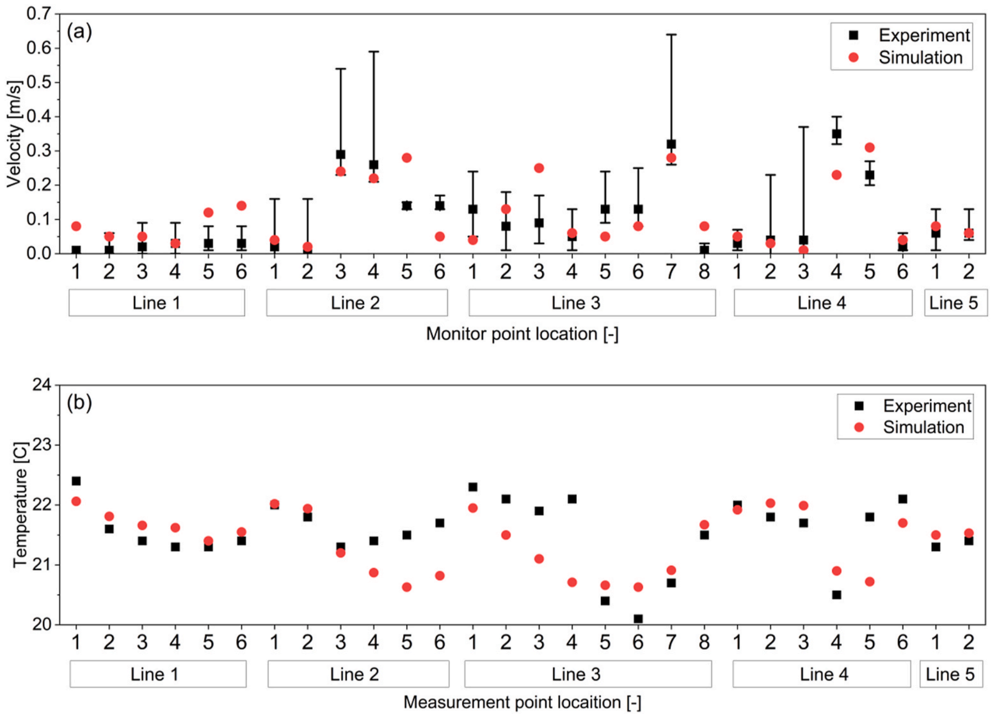

Fig. 4. a) validation of the airflow field through a comparison of velocity data, and b) validation of the thermal environment through a comparison of temperature data. The monitor points are numbered according to Fig. 3, arranged from left to right, with emphasis solely on those marked in red. (For interpretation of the references to colour in this figure legend, the reader is referred to the Web version of this article.)

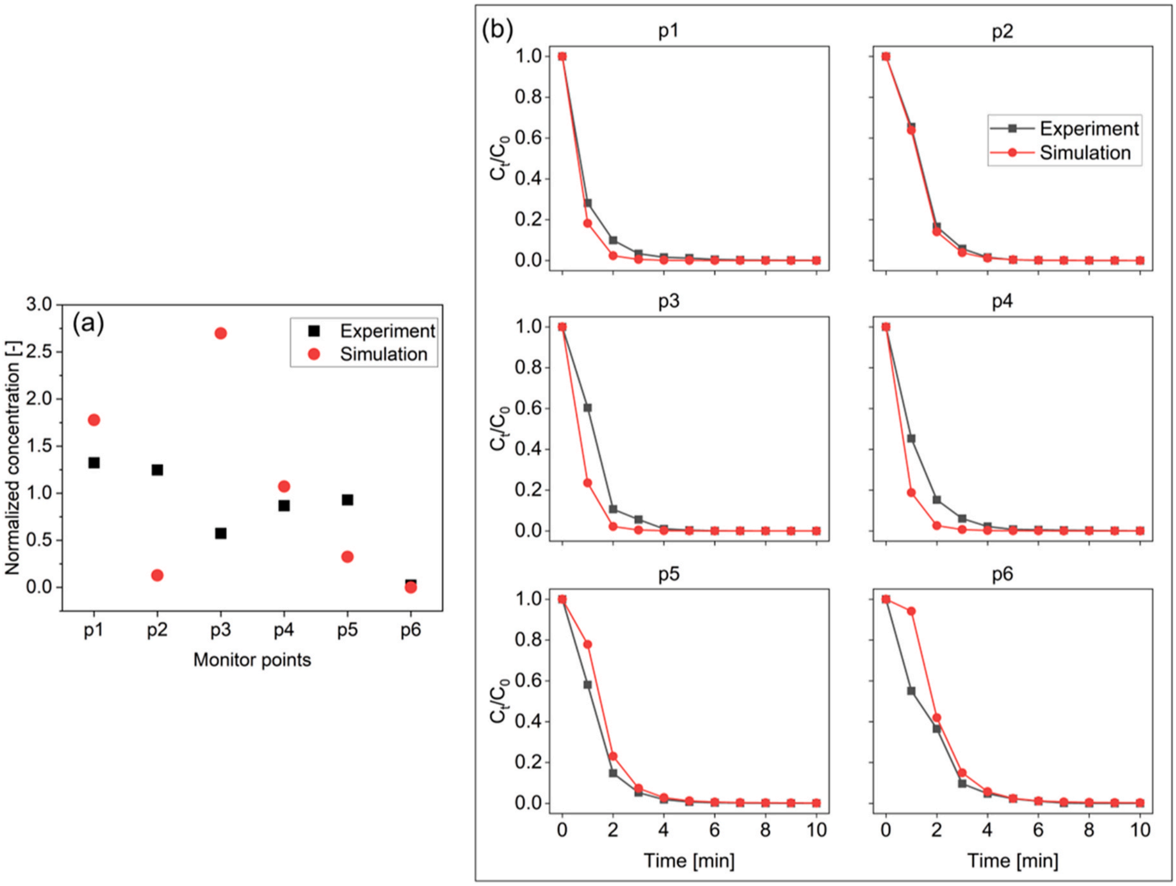

Fig. 5. a) The steady-state contaminant field validation, and b) The contaminant decay validation, where C_t represents the concentration after time t (minutes), and C_0 denotes the initial concentration.

Fig. 5 a illustrates the steady-state tracer concentration levels at the six designated locations, following several minutes of tracer injection at a release rate of 6.94e-7 kg/s. The experimental scenario revealed lower concentrations at points 1, 3, and 4, yet displayed higher values at points 2 and 5 compared to those in the simulation. This difference suggests an enhanced dispersion of contaminants into the OR's interior during the experimental phase, possibly due to door openings required for laboratory personnel to activate or deactivate experimental apparatus. These unavoidable behaviors have posed challenges to maintain a steady state during measurements, leading to significant deviations from the simulated result, especially at the location of p2 and p3. To minimize the potential distortion, the data for these two points are excluded for the quantitative error analysis. The Root Mean Square Error (RMSE) of normalized particle concentration for the rest four locations is calculated as 0.39. Compared to literature data [36], this deviation level is within the acceptable range.

Evaluating the TcAF system's contaminant removal efficiency necessitates a numerical model that precisely mirrors the decay process. Fig. 5 b shows good agreement between the simulated and experimental outcomes in terms of the tracer concentration changes over a 10-min decay interval. This temporal variation is quantified into the index of cleanliness decay rate. Table 3 shows the quantitative comparison between the measured and simulated contaminant decay rates at different monitor points. The maximum relative error of 16 %, aligns with the uncertainty levels reported in other literature.

Various studies have elucidated that factors such as the background contaminant concentration, uncertainties associated with measurement equipment, and human elements can significantly impact the accuracy of particle dispersion experiments, thereby complicating the validation of the contaminant field [37–40]. Considering these factors, the alignment observed between the experimental and simulated tracer concentrations in this study is deemed acceptable and sufficiently validated.

Upon a thorough evaluation of both the airflow and contaminant dispersion fields, it is concluded that the simulation model employed in this research is aptly suited for exploring the dynamics within an OR equipped with the TcAF system.

3.2. Contaminant removal and dispersion under point sources

To assess the TcAF system's capability in addressing passive contaminant releases from diverse locations, the validated numerical model was employed to simulate twelve distinct scenarios, each featuring pollutants originating from individual release points, as depicted in Fig. 6. The complex airflow patterns and contaminant distributions encountered were encapsulated into various indices, designed to quantify the concentration levels and spatial distribution of contaminants, respectively.

3.2.1. SVE1: spatial average contaminant concentration

To quantify the dispersion of contaminants across various release points, the spatial average contaminant concentration, denoted as SVE1, was calculated for different scenarios. These calculations have been synthesized and are presented in Table 4.

In general, case studies reveal that lower SVE1 values are typically observed when contaminants are released from points situated in the OR's periphery compared to those cases where pollutants are introduced in the central zone. This phenomenon can be attributed to the superior efficiency of contaminant extraction by exhaust outlets over the pollutant sweeping capabilities of the UDAF21 system, which comprises three unidirectional airflow (UDAF) plenums positioned above the surgical area. Contaminants originating from periphery benefit from a shorter transit to exhausts, facilitating quicker removal and resulting in lower concentration levels. Conversely, central zone releases encounter longer paths to exit, compounded by obstructions like the surgical lamp and operating table that disrupt the unidirectional downward airflow, leading to insufficient air movement and potential contaminant accumulation.

Beyond physical locations, the local airflow structures markedly influence SVE1 values [17,41]. Notably, the SVE1 values for cases E3 and E6 stand at 1.75 and 1.30, respectively, significantly surpassing the average SVE1 value (0.67) recorded for other periphery scenarios. Fig. 7 delineates the velocity and streamline distribution in plane A-A, highlighting the positioning of points E3 and E6.

The internal 'laminar' air supply within the OR interacts with the operating table, causing a shift in the airflow stream from a vertical orientation to a horizontal one, which then spreads along the long side of the table. The high momentum of the incoming airflow, combined with the operating table's substantial length-to-width ratio, ensures that the outflow maintains its horizontal trajectory upon departing the long plate. Upon reaching the side walls, the airflow deflects, curling back to create nearby circulation. This specific airflow pattern establishes a

Table 3
Measured and simulated contaminant decay rates at six monitor points.

Cases	Contaminant decay rate [min^{-1}]		Percentage error [−]
	Measured	Simulated	
p1	0.75	0.85	12 %
p2	1.02	0.98	4 %
p3	1.21	1.40	16 %
p4	0.74	0.86	17 %
p5	0.99	1.03	5 %
p6	1.26	1.45	15 %

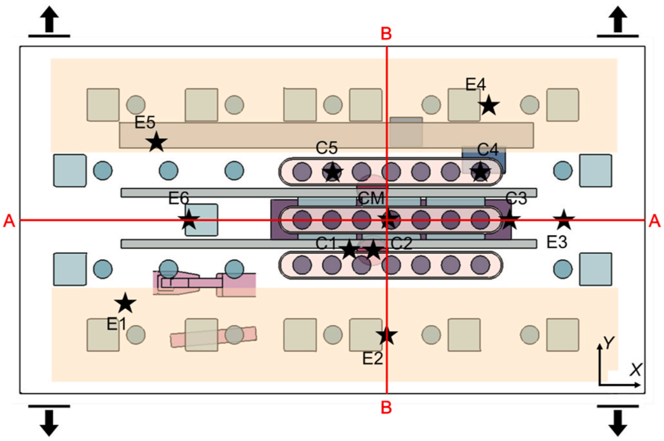

Fig. 6. The location of contaminant injection for 12 cases. Points labeled with 'E' signify particle releases in the periphery zone, whereas points prefixed with 'C' indicate releases in the central area of the OR. The diagram also features two vertical planes: A-A, positioned at y = 3.25 m, and B–B, situated at x = 6.9 m, providing a reference for the spatial orientation. Yellow boxes delineate the areas extending outward along the long side of the operating table, offering a visual guide to the spatial configuration under investigation. (For interpretation of the references to colour in this figure legend, the reader is referred to the Web version of this article.)

Table 4
The SVE1 values for the 12 cases studied. Values highlighted in red font signify outliers within each group, providing insights into the variability and extremities of contaminant distribution under different conditions.

Group	Location						Average value (Excluding outliers)
Periphery	E1	E2	E3	E4	E5	E6	0.67
	0.50	0.80	1.75	0.66	0.74	1.30	
Central zone	CM	C1	C2	C3	C4	C5	0.95
	1.03	0.83	0.92	1.04	0.49	0.61	

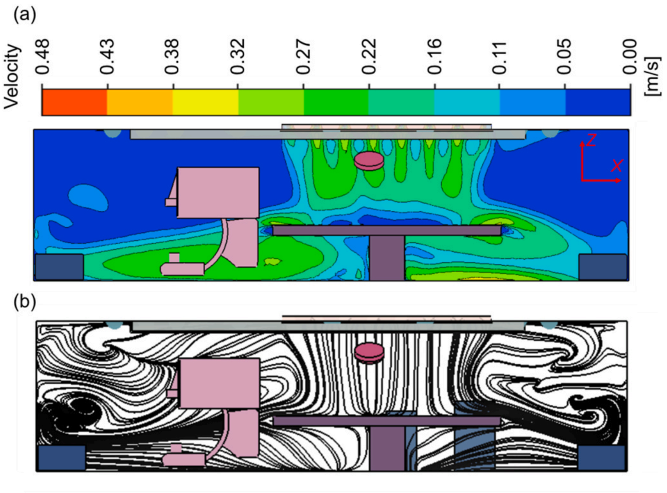

Fig. 7. The airflow pattern in Plane A–A: a) velocity contour plot, b) streamline distribution.

barrier, inhibiting vertical air and contaminant mixing on both sides of the operating table along the X-axis. Given the placement of exhaust vents at floor level, contaminants released above this airflow barrier—particularly in cases E3 and E6—experience delayed removal from the OR. Case E3 is further exacerbated by the constrained space on the table's right side, which intensifies the airflow barrier effect. In the Y-axis direction, exemplified by case E2 (illustrated in Fig. 8), the inflowing air navigates around the obstruction, reaching down to floor level. However, the transition from vertical to horizontal directionality is less pronounced due to the obstacle's relatively narrow width.

In the space extending outward along the long edge of the OR table, marked by yellow boxes in Fig. 6, there is ample room, ensuring that contaminant diffusion is not restricted. Consequently, this spatial arrangement does not significantly influence pollutant discharge. As for contaminant releases in the central zone, particularly cases C4 and C5, they exhibit notably low SVE1 values (0.49 and 0.61). They are located in the outer part of the UDAF 21 area. Analysis of Fig. 8 reveals that this region benefits from a robust air supply and minimal streamline deformation. Owing to the minimal obstruction and prevailing unidirectional airflow, case C4 records the lowest SVE1 among the twelve-point source scenarios studied. The slightly higher SVE1 value for case C5, compared to case C4, is attributed to its greater distance from the exhaust vents.

For other central zone locations (CM – C2), under-table flow circulation tends to accumulate tracer particles, resulting in elevated spatial average contaminant concentration (SVE1) levels. This comprehensive assessment of SVE1 underscores the variability in contaminant removal efficiency across different locations, illustrating a clear correlation between SVE1 values and proximity to exhaust outlets. Contaminants originating from the OR's outer regions, closer to the outlets, typically undergo a quicker removal process, leading to lower room-average pollutant concentrations. In the case of central area releases, the forceful momentum of airflow flushing mitigates the disadvantages of distance from exhaust outlets, achieving low spatial average concentration levels. However, this dynamic is susceptible to disruption by obstacles. Specifically, the operating table obstructs internal downward air jets, redirecting high-speed airflow laterally. This air barrier hampers vertical mixing, rendering the upper periphery of the OR less effective in contaminant removal.

3.2.2. G and SVE2: spatial extent of contaminant dispersion

Building upon the simulations described in section 3.2.1, the characterization of passive contaminant dispersion, is quantified through two distinct indices: G and SVE2. The method of quantification draws an analogy with the concept of a probability density function, where G signifies the mean of the distribution, and SVE2 denotes its variance.

Fig. 9 presents an isosurface visualization that captures varying levels of contaminant concentration. Originating from the point of release, contaminant concentrations exhibit a gradual decline. Influenced by both convection and diffusion, the contaminants disperse in all directions, displaying varying intensities, which culminate in the formation of these three-dimensional irregular isosurfaces.

Considering the space enclosed by isosurfaces as representing an inhomogeneous substance, the center of gravity G functions as the mass centroid, pinpointing the primary concentration of mass, while the release point denotes the area of highest density. With G established as the reference point, the 3D spatial spread of contaminants is characterized by a key dimension, SVE2, representing the mean dispersion radius $\sqrt{\left(R^{x^2}+R_y^2+R_z^2\right)}$.

Fig. 10 illustrates the deviation between the concentration centroid and the contaminant source across 12 simulation scenarios. A comparison between cases of internal releases and those originating from the external periphery reveals that internal cases exhibit significantly larger deviation distances. The dynamic fluid motion induced by UDAF21 facilitates a robust flushing effect, swiftly moving contaminants away from the central critical zone (the source location). Assisted by exhaust outlets, pollutants are efficiently directed and subsequently evacuated from the OR. The directionality of the arrows in the xy plane elucidates the primary path through which contaminants are expelled, indicating the prevailing trend of dispersion. The vertical deviation direction further underscores distinct dynamics between external and internal release scenarios. Central releases predominantly exhibit a downward trajectory, whereas the dispersion of peripheral contaminants is shaped by their proximity to exhaust outlets and the prevailing local airflow patterns. When examining individual release points, nuanced differences become apparent. For instance, C3, due to its intermediary position, does not exhibit enhanced contaminant transport compared to other internal points. Influenced by surgical lamps, case C2 shows a reduced vertical deviation relative to the adjacent C3 case. As for case E3, contaminants tend to accumulate above the release point. The air barrier effect—resulting from a potent central air supply and the extensive operating table—overriding the pressure gradient from inlets to outlets, thus manifesting an atypical upward vertical deviation.

The spatial extent of contaminant dispersion, quantified by SVE2 for

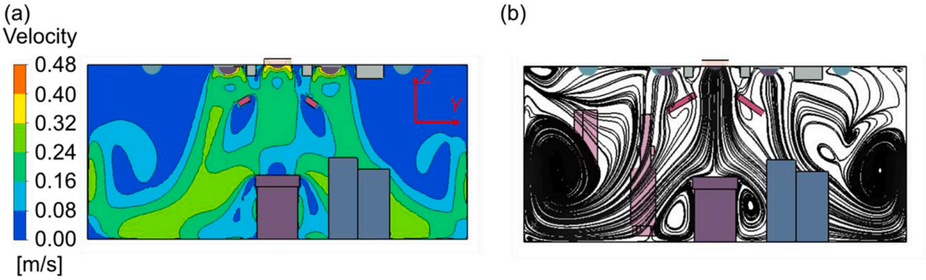

Fig. 8. The airflow pattern in Plane B–B: a) velocity distribution, b) streamline distribution.

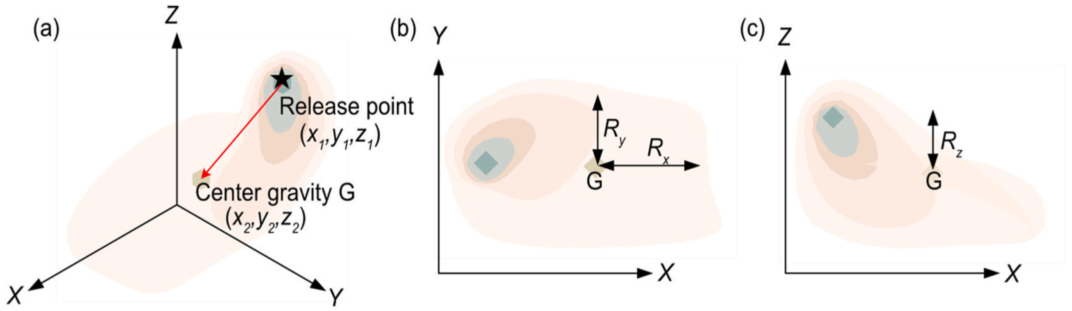

Fig. 9. The dynamics of contaminant dispersion within a three-dimensional space, a) 3D diagram, release point (x_1,y_1,z_1) and center gravity G (x_2,y_2,z_2), b) the projection in xy plane, R_x: the component of mean dispersion radius in the x direction, R_y: the radius component in the y direction, c) the projection in xz plane, R_z: the radius component in the z direction.

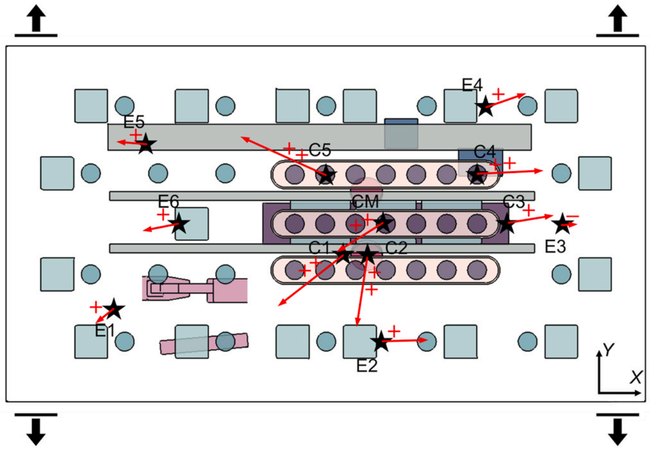

Fig. 10. The deviation between each release point and the corresponding center of gravity G. The length of each arrow signifies the distance between these two points, while the arrow's direction indicates the orientation of dispersion in the xy plane. The symbols '+' or '-' denote the degree of deviation in the z-direction, offering insights into the vertical spread of contaminants.

the 12 individual point injection cases, is detailed in Table 5. It is noted that a proximity to exhaust outlets is associated with a reduced dispersion radius, underscoring the role of the migration process—from source to exit—in contaminant removal. Central zone cases CM, C1, C2, and C5 exhibit enlarged dispersion distances due to their considerable separation from exhaust outlets. Periphery cases E2 and E6, situated between exhaust outlets, demonstrate extensive spread in both horizontal and vertical directions, reflected in larger SVE2 values. As for cases C3, C4, and E3, the constrained space on the right side dispersion, resulting in a more compact spatial extent. These findings affirm the pivotal influence of physical location on SVE2. However, the effect of local airflow patterns, shaped by the ventilation system, on dispersion dynamics remains indistinct.

In this section, we explore 12 contaminant fields within the standard operation of the TcAF system. Each scenario involves generating contaminants from a single, precisely identified point. The objective is to illuminate the characteristics of local contaminant removal and dispersion through these representative cases. Thus, the analysis of distinct contaminant fields encompasses two dimensions: spatial average concentration level and range of spatial spread. The SVE1 index, indicating the mean contaminant concentration within the room, serves as a direct measure of local contaminant removal capability [17,42]. A lower SVE1 value, given a consistent contaminant generation rate, signifies enhanced pollutant removal from the environment. Conversely, G and SVE2 indices quantify the extent of contaminant displacement and distribution within the room, respectively, shedding light on dispersion characteristics across different locations [7,13,17]. A significant deviation between G and the contaminant source indicates rapid pollutant migration, whereas a minimal SVE2 value represents the pollutants are exhausted with limited diffusion.

Table 5
The VE2 values for the 12 cases, measured in meters.

Group	Location						Avg.
Periphery	E1	E2	E3	E4	E5	E6	1.56
	1.24	1.85	1.58	1.26	1.56	1.87	
Central zone	CM	C1	C2	C3	C4	C5	2.33
	3.26	2.66	2.59	1.50	1.55	2.39	

The evaluation of SVE1 demonstrates that contaminants released near exhaust outlets or beneath unobstructed internal air supplies are efficiently removed. Furthermore, the extraction effect of outlets is found to be more effective and consistent than the flushing impact of internal inlets. Air extraction via outlets has been validated as a potent mechanism for contaminant removal, with proximity to exhaust ports playing a crucial role in ensuring optimal efficiency [43,44]. As the distance from exhausts extends, extraction efficacy wanes, and the role of intricate local air patterns becomes predominant. Unidirectional air jets, a strategy commonly employed in controlled environments such as clean rooms, intensive care units, and ORs, are recognized for their washing/sweeping effect [45,46]. Within an OR utilizing the TcAF system, the internal high-momentum air supply is instrumental in maintaining air cleanliness, especially around UDAF 21. However, obstructions from subjects and thermal plumes significantly impact the performance of unidirectional downward airflow [47–50]. Ideal parallel streamlines are disrupted by obstacles, leading to unexpected mixing and inconsistent contaminant removal within the internal air supply zone. Achieving comparable SVE1 levels to scenarios near exhausts requires central locations to be enveloped in sufficiently filtered air, free from nearby obstructions—a challenging criterion during surgical operations.

Based on the analysis from SVE1, the superiority of contaminant control performance in the central zone compared to the periphery is not clear. This finding is inconsistent with previous literature [10,11], all of which have confirmed lower pollutant levels in the central zone. The reason for this discrepancy is that SVE1 is based on overall room averages, sacrificing some of the spatially uneven characteristics. It is possible that when pollutants are released from the center of the room and escape into the surrounding areas, they are not effectively removed, resulting in higher boundary concentrations and consequently increasing the overall pollutant concentration levels in the room. In pursuit of creating an ultra-clean environment throughout ORs, SVE1 remains an appropriate parameter, but it is not suitable for quantifying the performance of local areas.

During the spatial extent analysis, the authors discovered that the deviation between G (the center of gravity for contaminant distribution) and the release point offers more insight into airflow patterns and contaminant dispersions than does SVE2. The magnitude of this deviation illustrates the contaminant transport characteristics—whether they are predominantly convective or diffusive—while the direction of deviation indicates whether contaminant removal is facilitated or hindered. In the internal section of the OR, characterized by strong forced convection, substantial deviations with a pronounced downward direction were observed, indicating that contaminants are effectively swept away by the internal airflow. Conversely, in periphery cases, deviations were smaller and exhibited less vertical orientation, reflecting a less active contaminant transmission due to mixed air movements.

The disparity in contaminant dispersion characteristics between the internal and external sections of the OR is pronounced. Regarding SVE2, which is closely linked to the physical location of the contaminant release point, it was found that ample space around the release point results in larger SVE2 values. Contaminants released in central areas, equidistant from outlets, tend to disperse in all directions, whereas those released in corners primarily spread in one direction in a more confined manner. However, the distinct deviation distances from the release point can obscure local contaminant spread features. The reliability of SVE2 as a metric for assessing contaminant distribution has been critiqued by Essa et al. [51], who noted that each SVE2 value is normalized by individual concentration integral values (C_0 in Eq. (10)), leading to varied spatial extent scale criteria across different cases. Relying solely on SVE2 for case comparison may yield misleading interpretations.

3.3. *Age of the air*

The concept of "age of the air" or Air Change Effectiveness (ACE) is frequently utilized during the design phase, particularly when the specifics of contaminant release and room usage remain undetermined [33]. Unlike SVE1, G, and SVE2, which serve as quantitative indices for specific cases, the age of the air or ACE offers a more instructive and generalizable perspective [52]. To investigate the correlation with the indices discussed in Section 3.2, the ACE values for 12 distinct contaminant release locations are presented in Table 6.

The analysis reveals a spatial correlation between Air Change Effectiveness (ACE) and spatial average contaminant concentration (SVE1). Specifically, locations exhibiting lower ACE levels tend to have higher SVE1 values, exemplified by E3 in the periphery and C3 in the central zone. Similar to the findings from the analysis of the center of gravity (G) and mean dispersion radius (SVE2), the ACE assessment underscores a notable distinction between the internal and external air supply sections. This difference is particularly stark in ACE measurements, with the central zone demonstrating significant advantages over the periphery zone. However, there isn't a straightforward correlation among ACE, SVE1, G, and SVE2 values. Regions characterized by suboptimal airflow patterns are readily identifiable by their ACE values, which typically correlate with elevated room-averaged contaminant concentrations and inefficient dispersion. Nonetheless, high ACE levels do not inherently ensure effective contaminant control, especially in the presence of sources. While the assessment of ACE distribution aids in design optimization, it also presents notable limitations [33,52].

Thus, the air age theory or the ACE index is utilized in this subsection for a preliminary examination of how deviations from standard air supply configurations affect the potential for contaminant control throughout the OR. This evaluation includes comparing the volume-averaged ACE across different regions of the OR under varying ventilation rates. Additionally, the local air age patterns at a critical juncture, plane A-A, are visualized to highlight the distinctions among cases. Table 7 outlines the ventilation parameters across five simulation scenarios, including a breakdown of the regional divisions. The initial three cases feature total ventilation rates set at standard, modest, and low levels, respectively, maintaining a 1:1 fresh air volume ratio for areas A and B. The final two scenarios operate with a modest ventilation volume but with imbalanced air supply ratios between the central and periphery zones.

Table 6
Air Change Effectiveness (ACE) values at 12 locations with Standard Ventilation Rate.

Group	Location					
Periphery	E1	E2	E3	E4	E5	E6
	1.94	1.31	0.98	1.40	2.18	1.57
Central zone	CM	C1	C2	C3	C4	C5
	9.01	8.76	5.93	1.08	3.57	8.10

The analysis reveals that preferential air supply from the internal section facilitates fresh air replacement at a rate 2–3 times faster than what is observed in a perfectly mixed scenario (ACE = 1), highlighting the efficiency of unidirectional airflow with minimal mixing or diffusion. An ACE value of approximately 1 in area B signifies the presence of mixed flow in the periphery. Given that the peripheral region encompasses most of the OR's volume, the trend of the average ACE in area AB aligns closely with that observed in area B, indicating that the room volume with an ACE greater than 1 correlates with the peripheral ACE level. Consequently, a higher ACE value in the periphery indicates a larger volume that is effectively ventilated.

Fig. 11 a demonstrates the air change performance in the central area is highly responsive to variations in the total ventilation rate, whereas the periphery zone's performance remains largely stable despite reductions in ventilation volume. The presence of strong downward airflow in the central area underpins its superior ventilation performance. Incremental enhancements in external airflow supply, as depicted in Fig. 11 b, may slightly increase the volume with an ACE greater than 1. However, such adjustments are unlikely to alter the fundamentally mixed airflow characteristics of this region, with the average ACE remaining approximately 1.

Case 4 aims to sustain the strong downward airflow in the central zone while reducing the peripheral airflow rate to half its original value. Despite maintaining the same total ventilation volume as case 2, the overall Air Change Effectiveness (ACE) level sees a 16 % reduction. This decrease in ACE, attributed to inadequate air change in the periphery, is vividly illustrated in Fig. 12 d. With the initial momentum flux diminished, the airflow from decentralized peripheral diffusers becomes further weakened and increasingly prone to obstruction. This results in insufficient ventilation in the external section and disruption of the internal air barrier, fostering a large stale air zone in the upper periphery of the OR. Consequently, contaminants are likely to accumulate around the operating table, posing a risk of encroaching into the central critical zone. Adjustments to air supply rates in case 4 exacerbate the imbalance between the two sections, thwarting efforts to establish an ultra-clean environment throughout the OR.

In contrast, case 5 presents a reversed scenario in which the internal airflow rate is halved, while the external ventilation rate remains at 350 m^3/h. As anticipated, the average ACE in area A decreases due to the reduced internal air supply. Nonetheless, the periphery zone achieves the highest ACE level under a modest total ventilation volume. Fig. 12 e depicts the air-age field for case 5, showing that the increased airflow rate in the periphery significantly expands the area with a modest air age. Most air around the operating table can be replaced with fresh air within 50 s, indicating a quicker response to potential passive pollutants compared to case 2. Notably, the air barrier effect along the operating table is less pronounced in case 5, resulting in a weaker hindrance to contaminant mixing in the periphery zone. The contour lines exhibit a smooth spreading pattern without the marked bumps and depressions seen in cases 1–3. Areas of inefficient ventilation are confined to near the room walls, distant from air terminal devices.

A comparative analysis of the five cases consistently demonstrates that the center area of the operating room (OR) maintains a lower age of the air compared to the periphery zone. This pattern arises due to the centralized placement of internal diffusers, contrasted with the decentralized installation of external air terminals. Notably, this characteristic

Table 7
Ventilation parameters of five simulation scenarios.

Case No.	Total airflow [m^3/h]	Ratio of area A, B	Airflow of each airshower [m^3/h]	Nominal age of the air [s]	Avg. ACE of area A	Avg. ACE of area B	Avg. ACE of area AB	Volume with ACE>1 [m^3]
Case 1	12600	1:1	300/350	64	3.69	1.16	1.27	183.22
Case 2	9450	1:1	225/262.5	85	3.15	1.07	1.17	177.57
Case 3	6300	1:1	150/175	127	2.38	1.00	1.09	173.69
Case 4	9450	2:1	300/175	85	3.30	0.89	0.98	161.80
Case 5	9450	1:2	150/350	85	2.86	1.23	1.32	190.31

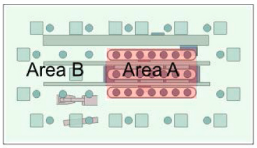

The top view delineates the boundaries of areas A and B. Area A corresponds to the central region, defined as the room volume beneath the internal air supply section. Conversely, Area B designates the periphery zone, representing the room volume beneath the external air supply section. Area AB encompasses both Area A and Area B, collectively representing the entirety of the OR.

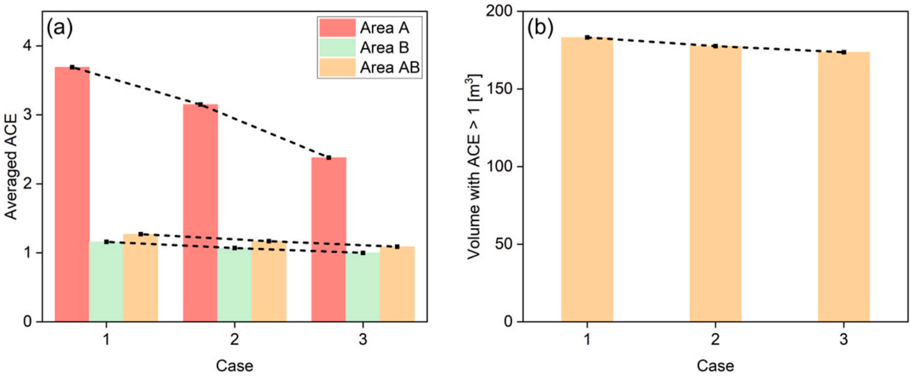

Fig. 11. The variation of two ventilation indices with the reduction of total ventilation rates: a). The volume-averaged ACE of three regions under different ventilation rates, b). The room volume with ACE>1 in the OR under different ventilation rates.

of airflow persists even in the face of inadequate or imbalanced air supply rates. The ventilation efficacy in the central zone is predominantly influenced by the absolute volume of air supplied. In contrast, the efficiency of ventilation in the periphery zone hinges on maintaining an optimal ratio of air supply between the internal and external sections, that is, the relative volume of air provided.

The dynamic of high-momentum airflow encountering various obstructions within the OR's critical zone leads to its redirection towards the periphery, thereby disrupting the initially low-speed mixing flow typical of this region. Strategies that increase the proportion of air supply directed to the external section have been recognized as beneficial, serving to diminish the air barrier effect and enhance the overall ventilation performance of the OR.

4. Conclusion

This study presents a pioneering investigation into the contaminant control performance of a novel hybrid ventilation scheme, the temperature-controlled airflow (TcAF) systems, through both experimental and numerical analyses. It elucidates the contaminant removal capabilities and the characteristics of spatial spread across different locations under the TcAF system, as well as detailing the air exchange performance under conditions of insufficient and imbalanced air supply. The key findings and recommendations are summarized as follows.

1. Effective management of point contaminant sources in ORs ventilated by the TcAF system necessitates leveraging the exhaust ports' extraction effect and the internal air showers' flushing effect. In the periphery zone, where air mixing prevails, proximity to outlets correlates with lower contaminant concentrations and reduced dispersion ranges. Positioning contaminant sources near exhaust ports is more advisable. In the central zone, where high-momentum air is introduced, avoiding obstacles is crucial for optimal contaminant control, and implementing localized exhaust can be effective.
2. The standard airflow configuration ensures a near-piston flow above the operating table and a mixing flow in the periphery zone. Optimal ventilation in the critical zone is achieved by supplying an adequate volume of fresh air, while the performance in the periphery zone depends on a balanced ratio between internal and external air supplies. Insufficient air supply, particularly when fresh air is concentrated in the central area, compromises contaminant control in the periphery. Conversely, ensuring an adequate airflow rate for external air showers can expand the ultra-clean area and mitigate the disruption caused by internal airflow on external low-speed air mixing. Additionally, adjusting the air supply configuration, such as centralizing the air shower in the periphery zone, can be considered as a strategy to overcome the disruptions.
3. SVE1 and G are suitable for evaluating contaminant removal and spread under specific point source scenarios. SVE2, significantly affected by physical location and the deviation between G and the release point, renders spatial extent characterization less clear. Relying solely on SVE2 and aiming for the smallest possible value without considering the employed ventilation scheme is impractical.
4. The ACE index can effectively quantify airflow patterns, independent of contaminant nature, making it valuable for identifying potential contamination zones and optimizing ventilation design. However,

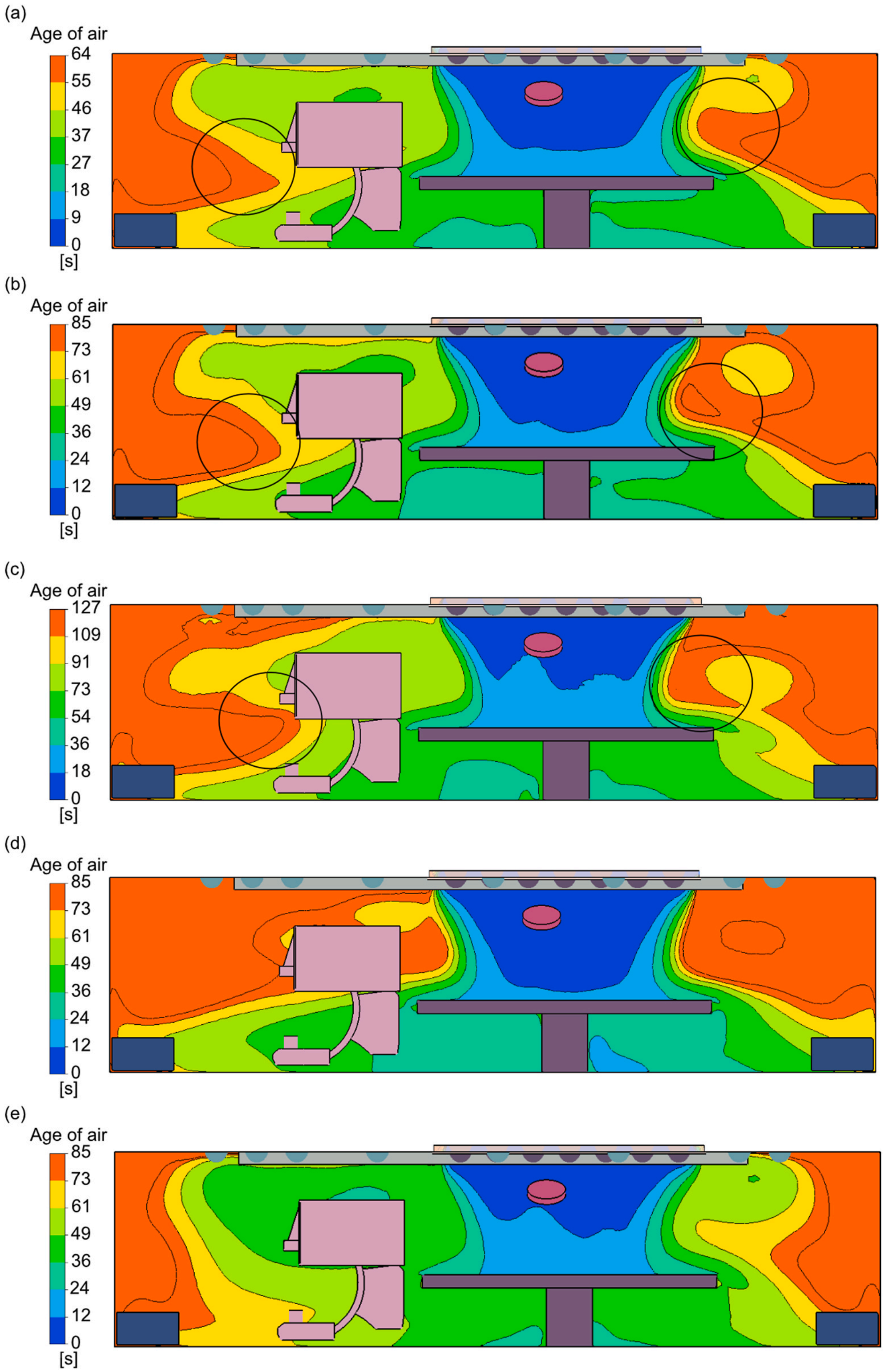

Fig. 12. The distribution of the local age of the air across the plane at y = 3.25 m for cases 1 through 5. The legend for this figure is calibrated to range from 0 to an upper limit, with the specific range denoted as (0, τ_n). Areas highlighted in orange on the graph represent regions where the Air Change Effectiveness (ACE) value is less than 1, indicating zones of relatively lower air change efficiency. (For interpretation of the references to colour in this figure legend, the reader is referred to the Web version of this article.)

ACE analysis tends to overemphasize the superiority of the internal air supply in contaminant control.

In terms of future works, the authors will continue with a quantitative assessment of ventilation performance regarding the contaminant control aspect. More factors will be included such as obstacles, contaminant types, etc. For obstacles that are relatively fixed in position, our focus will be on optimizing the configuration of inlets and outlets to overcome potential airflow distortion. For obstacles that are mobile, such as healthcare personnel, our prospect is to reproduce the airflow and contaminant dispersion under the influence of moving objects, quantify the intensity and extent of contamination and propose corresponding optimization strategies. As for contaminant types, the authors intend to investigate how human skin shedding and surgical smoke disperse under the TcAF system. By addressing this aspect in future studies, we hope to advance our understanding and contribute to the improvement of airflow control mechanisms in indoor environments.

CRediT authorship contribution statement

Nan Hu: Writing – original draft, Visualization, Validation, Software, Methodology, Investigation, Conceptualization. **Jos Lans:** Writing – review & editing, Methodology, Conceptualization. **Annika Gram:** Writing – review & editing, Supervision. **Peter Luscuere:** Writing – review & editing. **Sasan Sadrizadeh:** Writing – review & editing, Supervision, Funding acquisition.

Declaration of competing interest

The authors declare the following financial interests/personal relationships which may be considered as potential competing interests:

Jos Lans is CEO of Medexs BV, a company that supplies and install OR ventilation systems. If there are other authors, they declare that they have no known competing financial interests or personal relationships that could have appeared to influence the work reported in this paper.

Data availability

Data will be made available on request.

Acknowledgment

This study was supported by the Swedish Research Council - Formas (Grant No. 2021-01422) and the China Scholarship Council (CSC) (No. 202108310037). Computational support was facilitated by the Swedish National Infrastructure for Computing (SNIC) at PDC Center for High-Performance Computing, KTH Royal Institute of Technology, under the auspices of the Swedish Research Council (Grant No. 2018-05973). The authors would also like to thank the staff of Rijnstate hospital Arnhem, the Netherlands, for making the operating rooms available for the measurements.

References

[1] M.J. Mukagendaneza, E. Munyaneza, E. Muhawenayo, D. Nyirasebura, E. Abahuje, J. Nyirigira, et al., Incidence, root causes, and outcomes of surgical site infections in a tertiary care hospital in Rwanda: a prospective observational cohort study, Patient Saf. Surg. 13 (2019) 10.
[2] L.M. O`Hara, K.A. Thom, M.A. Preas, Update to the centers for disease control and prevention and the healthcare infection control practices advisory committee guideline for the prevention of surgical site infection (2017): a summary, review, and strategies for implementation, Am. J. Infect. Control 46 (2018) 602–609.
[3] S.S. Magill, J.R. Edwards, W. Bamberg, Z.G. Beldavs, G. Dumyati, M.A. Kainer, et al., Multistate point-prevalence survey of health care-associated infections, N. Engl. J. Med. 370 (2014) 1198–1208.
[4] M. Cortale, V. Gobessi, L. Calligaris, [The role of the environment in postoperative infections], Ann. Ital. Chir. 60 (1989) 541–547.
[5] O.M. Lidwell, R.A. Elson, E.J. Lowbury, W. Whyte, R. Blowers, S.J. Stanley, et al., Ultraclean air and antibiotics for prevention of postoperative infection. A multicenter study of 8,052 joint replacement operations, Acta Orthop. Scand. 58 (1987) 4–13.
[6] T. Lipinski, D. Ahmad, N. Serey, H. Jouhara, Review of ventilation strategies to reduce the risk of disease transmission in high occupancy buildings, Int. J. Thermofluids 7–8 (2020) 100045.
[7] B. Yang, A.K. Melikov, A. Kabanshi, C. Zhang, F.S. Bauman, G. Cao, et al., A review of advanced air distribution methods - theory, practice, limitations and solutions, Energy Build. 202 (2019).
[8] S. Sadrizadeh, A. Aganovic, A. Bogdan, C. Wang, A. Afshari, A. Hartmann, et al., A systematic review of operating room ventilation, J. Build. Eng. 40 (2021).
[9] B.V.F. Silva, J.B. Holm-Nielsen, S. Sadrizadeh, M.P.R. Teles, M. Kiani-Moghaddam, A. Arabkoohsar, Sustainable, green, or smart? Pathways for energy-efficient healthcare buildings, Sustain. Cities Soc. 100 (2024) 105013.
[10] M. Alsved, A. Civilis, P. Ekolind, A. Tammelin, A.E. Andersson, J. Jakobsson, et al., Temperature-controlled airflow ventilation in operating rooms compared with laminar airflow and turbulent mixed airflow, J. Hosp. Infect. 98 (2018) 181–190.
[11] C. Wang, S. Holmberg, S. Sadrizadeh, Numerical study of temperature-controlled airflow in comparison with turbulent mixing and laminar airflow for operating room ventilation, Build. Environ. 144 (2018) 45–56.
[12] Z. Liu, H. Liu, H. Yin, R. Rong, G. Cao, Q. Deng, Prevention of surgical site infection under different ventilation systems in operating room environment, Front. Environ. Sci. Eng. 15 (2021).
[13] G. Cao, H. Awbi, R. Yao, Y. Fan, K. Sirén, R. Kosonen, et al., A review of the performance of different ventilation and airflow distribution systems in buildings, Build. Environ. 73 (2014) 171–186.
[14] Li Y, Fuchs L, Holmberg S. Methods for Predicting air change efficiency. Advances 151:.
[15] M.S.K. Chen, L.T. Fan, C.L. Hwang, E.S. Lee, Air flow models in a confined space a study in age distribution, Build. Sci. 4 (1969) 133–143.
[16] M. Sandberg, M. Sjoberg, The use of moments for assessing air quality in ventilated rooms, Build. Environ. 18 (1983) 181–197.
[17] S. Kato, S. Murakami, New ventilation efficiency scales based on spatial distribution of contaminant concentration aided by numerical simulation, Build. Eng. 94 (1988) 309–330.
[18] S. Kato, S. Murakami, H. Kobayashi, Scales for Evaluating Ventilation Efficiency as, 1992, pp. 321–332.
[19] D. Etheridge, M. Sandberg, Building Ventilation: Theory and Measurement, 1996.
[20] C. Federspiel, Air-change effectiveness : theory and calculation, Indoor Air (1999) 47–56.
[21] E. Lim, K. Ito, M. Sandberg, Performance evaluation of contaminant removal and air quality control for local ventilation systems using the ventilation index Net Escape Velocity, Build. Environ. 79 (2014) 78–89.
[22] K. Khankari, Analysis of Spread Index - A Measure of Laboratory Ventilation Effectiveness, 2018, pp. 1–8.
[23] X. Tian, S. Zhang, H.B. Awbi, C. Liao, Y. Cheng, Z. Lin, Multi-indicator evaluation on ventilation effectiveness of three ventilation methods: an experimental study, Build. Environ. 180 (2020) 107015.
[24] Z.J. Zhai, Z. Zhang, W. Zhang, Q.Y. Chen, Evaluation of various turbulence models in predicting airflow and turbulence in enclosed environments by cfd: Part 1—summary of prevalent turbulence models, HVAC R Res. 13 (2007) 853–870.
[25] S. Sadrizadeh, A. Tammelin, P. Ekolind, S. Holmberg, Influence of staff number and internal constellation on surgical site infection in an operating room, Particuology 13 (2014) 42–51.
[26] T.T. Chow, X.Y. Yang, Performance of ventilation system in a non-standard operating room, Build. Environ. 38 (2003) 1401–1411.
[27] I. Ansys, ANSYS FLUENT Theory Guide, 794, Canonsburg, Pa, 2011.
[28] S. Marashian, S. Sadrizadeh, O. Abouali, Modeling particle distribution in a ventilated room with modified discrete random walk methods, Int. J. Vent. 22 (2023) 289–306.
[29] S. Li, J. Yang, Effects of inclination angles on stepped chute flows, Appl. Sci. 10 (2020).
[30] S. Li, J. Yang, X. Ma, X. Li, Flow features in a pooled fishway with V-shaped weir formation, Eng. Appl. Comput. Fluid Mech. 14 (2020) 1337–1350.
[31] E. Mundt, H.M. Mathisen, P.V. Nielsen, A. Moser, Ventilation Effectiveness, 2004.
[32] X. Li, D. Li, X. Yang, J. Yang, Total air age: an extension of the air age concept, Build. Environ. 38 (2003) 1263–1269.
[33] J.M. Villafruela, F. Castro, J.F. San José, J. Saint-Martin, Comparison of air change efficiency, contaminant removal effectiveness and infection risk as IAQ indices in isolation rooms, Energy Build. 57 (2013) 210–219.
[34] DIN 1946-4, 2008-9 Ventilation and Air Conditioning - Part 4: Ventilation in Buildings and Rooms of Health Care, 2018.
[35] ISO 14644-3:2019(en) Cleanrooms and associated controlled environments — Part 3: Test methods, 2019.
[36] Y.S. Eom, D.H. Kang, D. Rim, M. Yeo, Particle dispersion and removal associated with kitchen range hood and whole house ventilation system, Build. Environ. 230 (2023) 109986.
[37] Z. Zhang, X. Chen, S. Mazumdar, T. Zhang, Q. Chen, Experimental and numerical investigation of airflow and contaminant transport in an airliner cabin mockup, Build. Environ. 44 (2009) 85–94.
[38] W. Yan, Y. Zhang, Y. Sun, D. Li, Experimental and CFD study of unsteady airborne pollutant transport within an aircraft cabin mock-up, Build. Environ. 44 (2009) 34–43.
[39] Z. Liu, D. Yin, L. Hu, J. He, G. Cao, Bacteria-carrying particles diffusion in the operating room due to the interaction between human thermal plume and ventilation systems: an experimental-numerical simulation study, Energy Build. 270 (2022) 112277.
[40] Z. Ai, C.M. Mak, N. Gao, J. Niu, Tracer gas is a suitable surrogate of exhaled droplet nuclei for studying airborne transmission in the built environment, Build. Simulat. 13 (2020) 489–496.
[41] K.S. Lee, K.O. Lim, K.H. Ahn, Y.S. Jung, Numerical analysis of moisture ventilation in a lithium ion battery manufacturing dry room, Dry. Technol. 19 (2001) 455–470.
[42] S. Zhang, D. Niu, Y. Lu, Z. Lin, Contaminant removal and contaminant dispersion of air distribution for overall and local airborne infection risk controls, Sci. Total Environ. 833 (2022) 155173.
[43] Z. Younsi, L. Koufi, H. Naji, Numerical study of the effects of ventilated cavities outlet location on thermal comfort and air quality, Int. J. Numer. Methods Heat Fluid Flow 29 (2019) 4462–4483.

[44] J. Cho, Investigation on the contaminant distribution with improved ventilation system in hospital isolation rooms: effect of supply and exhaust air diffuser configurations, Appl. Therm. Eng. 148 (2019) 208–218.

[45] S. Sadrizadeh, S. Holmberg, A. Tammelin, A numerical investigation of vertical and horizontal laminar airflow ventilation in an operating room, Build. Environ. 82 (2014) 517–525.

[46] T. Lin, O.A. Zargar, K.Y. Lin, O. Juiña, D.L. Sabusap, S.C. Hu, et al., An experimental study of the flow characteristics and velocity fields in an operating room with laminar airflow ventilation, J. Build. Eng. 29 (2020) 1–9.

[47] Y.C. Tung, S.C. Hu, T. Xu, R.H. Wang, Influence of ventilation arrangements on particle removal in industrial cleanrooms with various tool coverage, Build. Simulat. 3 (2010) 3–13.

[48] G. Cao, A.M. Nilssen, Z. Cheng, L.I. Stenstad, A. Radtke, J.G. Skogås, Laminar airflow and mixing ventilation: which is better for operating room airflow distribution near an orthopedic surgical patient? Am. J. Infect. Control 47 (2019) 737–743.

[49] A. Aganovic, G. Cao, L.I. Stenstad, J.G. Skogås, An experimental study on the effects of positioning medical equipment on contaminant exposure of a patient in an operating room with unidirectional downflow, Build. Environ. 165 (2019) 106096.

[50] A. Aganovic, G. Cao, L.I. Stenstad, J.G. Skogås, Impact of surgical lights on the velocity distribution and airborne contamination level in an operating room with laminar airflow system, Build. Environ. 126 (2017) 42–53.

[51] A. Essa, T. Yamanaka, T. Kobayashi, N. Choi, Effect of source location on contaminant dispersion pattern and occupants inhaled air quality in lecture room under displacement ventilation. Japan Archit, Rev 6 (2023).

[52] A. Novoselac, J. Srebric, Comparison of air exchange efficiency and contaminant removal effectiveness as IAQ indices, Build. Eng. 109 (PART 2) (2003) 339–349.